nature photonics

ARTICLES

PUBLISHED ONLINE: 29 JUNE 2014 | DOI: 10.1038/NPHOTON.2014.138

# Integrated flexible chalcogenide glass photonic devices

Lan Li[1†], Hongtao Lin[1†], Shutao Qiao[2†], Yi Zou[1], Sylvain Danto[3], Kathleen Richardson[3,4], J. David Musgraves[4], Nanshu Lu[2] and Juejun Hu[1]*

**Photonic integration on thin flexible plastic substrates is important for emerging applications ranging from the realization of flexible interconnects to conformal sensors applied to the skin. Such devices are traditionally fabricated using pattern transfer, which is complicated and has limited integration capacity. Here, we report a convenient monolithic approach to realize flexible, integrated high-index-contrast chalcogenide glass photonic devices. By developing local neutral axis designs and suitable fabrication techniques, we realize a suite of photonic devices including waveguides, microdisk resonators, add–drop filters and photonic crystals that have excellent optical performance and mechanical flexibility, enabling repeated bending down to sub-millimetre radii without measurable performance degradation. The approach offers a facile fabrication route for three-dimensional high-index-contrast photonics that are difficult to create using traditional methods.**

Conventional on-chip photonic devices are fabricated almost exclusively on rigid substrates with little mechanical flexibility, but integration on deformable polymer substrates has given birth to flexible photonics, a field that has emerged rapidly in recent years to become the forefront of photonics research. By imparting mechanical flexibility to planar photonic structures, the technology has enormous application potential for aberration-free optical imaging[1], epidermal sensing[2], chip-to-chip interconnects[3] and broadband photonic tuning[4]. Free-space-coupled optical components including photodetectors[5], light-emitting diodes[6] and Fano reflectors[7] are among the first flexible semiconductor photonic devices to have been demonstrated. Planar integrated photonic structures such as microresonators and other waveguide-integrated devices potentially offer significantly improved performance characteristics compared to their free-space counterparts, because of their tight optical confinement and the facilitation of essential components for integrated photonic circuits. To date, flexible planar photonic devices have been fabricated almost exclusively using polymeric materials, which do not have the high refractive indices necessary for strong optical confinement. Silicon-based, high-index-contrast flexible waveguide devices were first demonstrated using a transfer printing approach[8]. However, this hybrid approach involves multiple pattern transfer steps between different substrates and has limited throughput, yield and integration capacity[9,10]. More recently, amorphous silicon devices have been fabricated via direct deposition and patterning[11]. However, the optical quality of the silicon material was severely compromised by the low deposition temperature dictated by the polymer substrate's thermal budget. Silicon nitride is another material candidate that does not require epitaxial growth on single-crystal substrates. However, polymer substrates cannot withstand the high deposition temperature of low-loss nitride in the low-pressure chemical vapour deposition process (>500 °C)[12], and silicon nitride deposited by sputtering or plasma-enhanced chemical vapour deposition (PECVD) generally exhibits high optical losses[13,14]. Oxynitride deposited via PECVD or sputtering may offer a viable route for flexible photonic device fabrication, although oxygen plasma damage to polymer substrates presents a challenge yet to be mitigated.

As well as these multimaterial integration challenges, planar integrated photonics stipulate a distinctively different set of requirements in their configurational design to achieve structural flexibility. For example, the neutral plane design widely adopted for flexible electronics[15,16] dictates that the device layer should be embedded inside the flexible substrate near the neutral plane to minimize strain exerted on the devices when the structure is deformed. However, encapsulation of the various photonic components deep within a thick top cladding layer prohibits effective heat dissipation as well as evanescent wave interactions with the external environment, an essential condition for biochemical sensing and evanescent optical coupling. To achieve efficient optical coupling, current flexible photonic devices are placed on the surface of polymer substrates. As a consequence, the devices are subjected to large strains upon bending and exhibit only moderate flexibility with a bending radius typically no less than 5 mm (refs 3,5,11). This mechanical performance severely limits the range of degrees of freedom available for deployment.

In this Article, we demonstrate monolithic photonic integration on plastic substrates using high-refractive-index chalcogenide glass (ChG) materials. This process yields high-index-contrast photonic devices with record optical performance and benefits significantly from improved processing protocols based on simple, low-cost contact lithography. We show that this versatile process can be readily adapted to different glass compositions with tailored optical properties to meet different candidate applications. A novel local-neutral-axis design is implemented to render the structure highly mechanically flexible, enabling repeated bending of the devices down to sub-millimetre bending radii without a measurable degradation in optical performance. We note that classical multilayer beam bending theory fails in our design due to the large modulus contrast among the different layers. For this reason, a new analytical model was developed to take into account the multiple neutral axes in a multilayer stack so as to successfully

[1]Department of Materials Science and Engineering, University of Delaware, Newark, Delaware 19716, USA, [2]Centre for Mechanics of Solids, Structures and Materials, Department of Aerospace Engineering and Engineering Mechanics, University of Texas at Austin, Austin, Texas 78712, USA, [3]College of Optics and Photonics, CREOL, Department of Materials Science and Engineering, University of Central Florida, Orlando, Florida 32816, USA, [4]IRradiance Glass Inc., Orlando, Florida 32828, USA; †These authors contributed equally to this work. *e-mail: hujuejun@udel.edu

NATURE PHOTONICS DOI: 10.1038/NPHOTON.2014.138

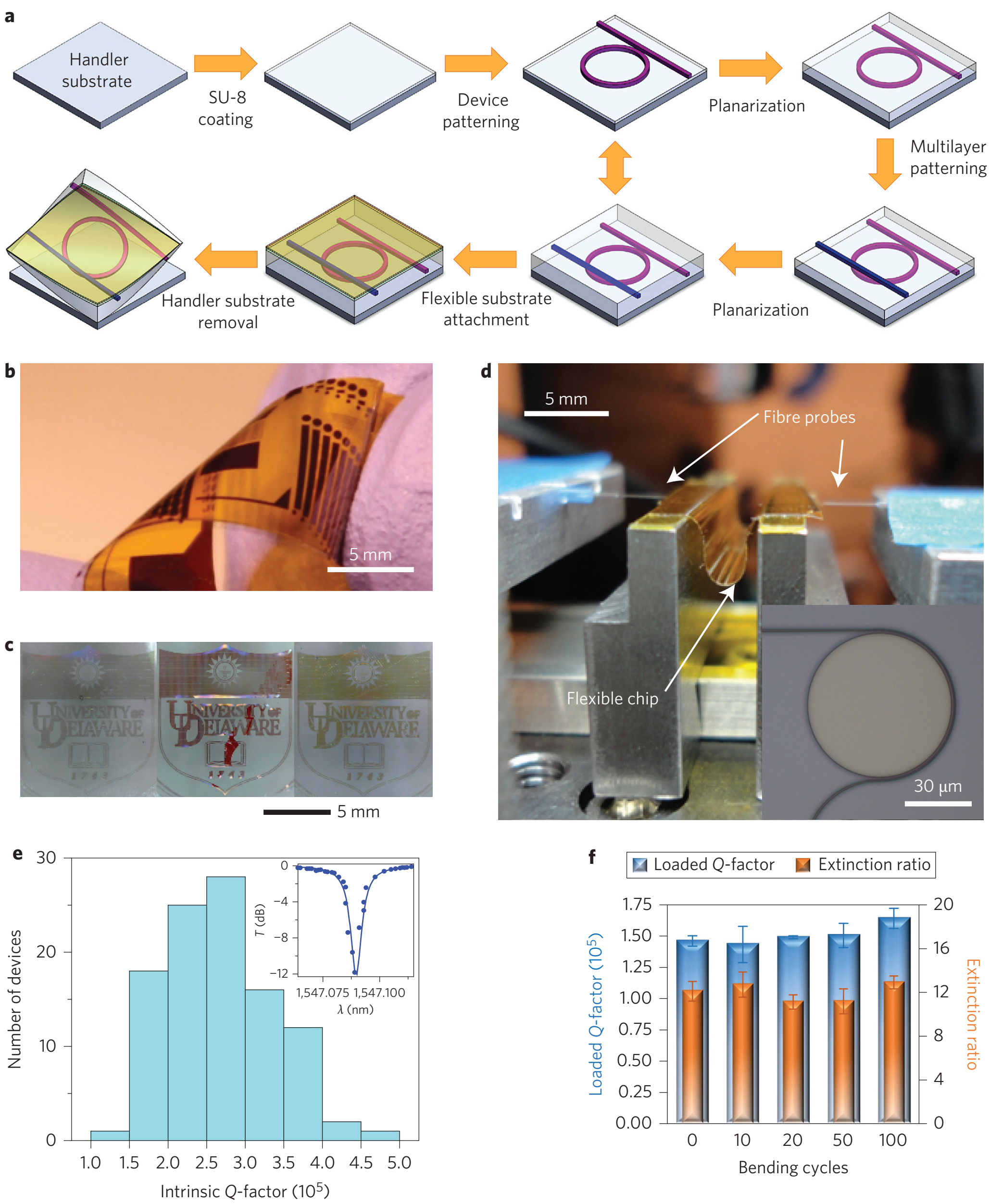


**Figure 1 | Flexible glass photonic device fabrication and mechanical reliability tests. a**, Schematic overview of the monolithic 3D flexible photonic device fabrication process. **b**, Photograph of a flexible photonic chip showing a linear array of microdisk resonators. **c**, University of Delaware logo on polydimethylsiloxane flexible substrates made of $Ge_{23}Sb_7S_{70}$, $As_2Se_3$ and $As_2S_3$ glasses (from left to right). **d**, Photograph of the fibre end-fire testing set-up used for *in situ* measurement of optical transmission characteristics during mechanical bending of the flexible devices. **e**, Intrinsic *Q*-factor distribution measured in flexible microdisk resonators. Inset: example of resonator transmission spectrum. **f**, Loaded *Q*-factors and extinction ratios of the resonator after multiple bending cycles at a bending radius of 0.5 mm.

capture the strain–optical coupling behaviour in our devices. We also further exploited the monolithic integration approach for three-dimensional (3D) multilayer fabrication. Compared to conventional 3D stacking methods involving wafer bonding[17], nanomanipulation[18], ion implantation[19], or multi-step chemical mechanical polishing[20], our approach offers a more simple and robust alternative route for novel 3D photonic structure processing.

## Device fabrication and mechanical reliability test

Figure 1a schematically illustrates our device fabrication process flow. The process begins by spin-coating epoxy (SU-8) onto a rigid handler (for example, an oxide coated Si wafer), followed by ChG evaporation deposition and liftoff patterning using ultraviolet contact lithography (see Methods). We chose ChGs as the photonic materials for several reasons, including their amorphous nature and low deposition temperature (allowing direct monolithic flexible substrate integration[21–24]), their high refractive indices (2–3, compatible with high-index-contrast photonic integration), and their almost infinite capacity for composition alloying (allowing fine-tuning of optical as well as thermomechanical properties over a broad range), making them suitable for diverse applications. SU-8 epoxy was used as the cladding polymer because of its proven chemical stability, excellent optical transparency and superior planarization capacity. Before ultraviolet exposure SU-8 epoxy behaves as a thermoplastic polymer amenable to thermal reflow treatments and the creation of a smooth surface finish, even on substrates with multilevel patterned structures. After thermal or ultraviolet cross-linking the epoxy becomes a thermosetting resin and is robust against mechanical deformation, humidity and subsequent thermal processing. Capitalizing on this unique property of SU-8, we developed an ultrathin epoxy planarization process with the high degree of planarization critical to 3D photonic integration. Details of the planarization process are described in Supplementary Section I. The deposition/patterning/planarization steps were repeated multiple times for 3D fabrication and no loss of degree of planarization was observed. Finally, the flexible samples were delaminated from the handler wafer using Kapton tape to form free-standing flexible structures. The Kapton tape consists of two layers, a silicone adhesive layer and a polyimide substrate, and has dual purposes: (1) it facilitates the delamination process and (2) the low-modulus silicone adhesive serves as an effective strain-relieving agent in our local-neutral-axis design (discussed in the following). Figure 1b presents a photograph of a final free-standing flexible photonic circuit chip. We have also tested the fabrication process with several different ChG compositions with vastly different optical properties (indices and Tauc optical bandgaps) to demonstrate the material compatibility of the process. Figure 1c shows University of Delaware logos patterned on flexible substrates with three different glass compositions: $Ge_{23}Sb_7S_{70}$ ($n$ = 2.1, $E_g$ = 2.2 eV)[25], $As_2Se_3$ ($n$ = 2.8, $E_g$ = 1.8 eV)[26] and $As_2S_3$ ($n$ = 2.4, $E_g$ = 2.1 eV)[27], all of which exhibit good adhesion to the SU-8 substrate. The inset in Fig. 1d shows a microscope image of a 30-μm-radius and 450-nm-thick $Ge_{23}Sb_7S_{70}$ microdisk resonator pulley coupled to an 800-nm-wide channel bus waveguide[28]. This simple fabrication route offers extremely high device yields; we have tested over 100 resonator devices randomly selected from samples fabricated in several different batches and all of them operated as designed after going through the entire fabrication process. Figure 1e plots the intrinsic $Q$-factor distribution of the devices measured near a wavelength of 1,550 nm, showing an average $Q$-factor of $(2.7 \pm 0.7) \times 10^5$, corresponding to an equivalent optical propagation loss of $1.6 \pm 0.4$ dB cm$^{-1}$ (Supplementary Fig. 2a). An example of a normalized resonator transmission spectrum is shown in the inset to Fig. 1e. Our best device exhibited an intrinsic $Q$-factor as high as 460,000, the highest value ever reported in photonic devices on plastic substrates.

A schematic illustration of the thickness profile of a fabricated flexible photonic chip is provided in Supplementary Fig. 6a. This photonic chip is composed of (top to bottom) a polyimide substrate, the silicone adhesive and the SU-8 cladding layer in which the devices are encapsulated. The notations are labelled in Supplementary Fig. 6a and tabulated in Supplementary Table 4. We experimentally measured the Young's moduli of the thin-film polyimide, silicone and SU-8 to be $E_1$ = 2.5 GPa, $E_2$ = 1.5 MPa and $E_3$ = 2 GPa, respectively (Supplementary Section IV). In the following we derive an analytical formula to predict the strain–optical coupling behaviour in the devices.

Classical beam bending theory predicts that when a multilayer structure is subject to pure bending, cross-sectional planes before bending are assumed to remain planar after bending and a unique neutral axis exists in the laminated structure (Supplementary Section V). However, the classical theory is only applicable to multilayer stacks where the layers have similar elastic stiffnesses. For the three-layer structure shown in Supplementary Fig. 6a, the Young's modulus of the silicone interlayer is three orders of magnitude smaller than that of the SU-8 or polyimide. When this sandwiched 'Oreo' structure is bent, the soft middle layer undergoes large shear deformation, which essentially decouples the deformation of the top and bottom stiff layers, similar to the strain decoupling effect discussed in the tension case[29]. As a result, each stiff layer has its own neutral axis and bending centre, and the stack thus demonstrates multiple neutral axes. We validated this postulate using both finite-element modelling (FEM) and an analytical multi-neutral axis theory, as discussed in Supplementary Section V. Because of the soft silicone interlayer, the location of the neutral axis can be shifted away from near the centre of the multilayer stack to within SU-8, a salient feature that enables photonic designs capitalizing on and enabling evanescent interactions while demonstrating extraordinary mechanical flexibility.

To experimentally validate the new theory, we performed strain–optical coupling measurements, where the optical resonant wavelengths of glass microdisk resonators were monitored *in situ* while the samples were bent. A block diagram of the home-built measurement set-up is illustrated in Supplementary Fig. 7a. Light from a tunable laser was coupled into the bus waveguides via fibre end-fire coupling, and the transmittance through the chip was monitored *in situ* as the samples were bent using linear motion stages. Figure 1d shows a flexible chip under testing. Further details regarding the measurement are provided in Supplementary Section VI.

The resonant wavelength shift $d\lambda$ can be expressed as a function of the local strain at the resonator, $d\varepsilon$:

$$\frac{d\lambda}{d\varepsilon} = \sum_i \left[ \frac{\lambda}{n_g} \cdot \Gamma_i \cdot \left( \frac{dn}{d\varepsilon} \right)_i \right] + \frac{n_{eff}}{n_g} \cdot \frac{\lambda}{L} \cdot \frac{dL}{d\varepsilon} + \frac{\lambda}{n_g} \cdot \frac{dn_{eff}}{d\varepsilon} \qquad (1)$$

where $\Gamma_i$ and $(dn/d\varepsilon)_i$ are the optical confinement factor and strain–optic coefficient in the $i$th cavity material, $L$ is the cavity length, and $n_g$ and $n_{eff}$ denote the group and effective indices, respectively. In equation (1), the first term on the right-hand side represents the optoelastic (that is, strain–optic) material response, the second term manifests the cavity length change, and the third term results from the cavity cross-sectional geometry modification. Derivation of the equation follows ref. 11 and is elaborated in Supplementary Section VII. Because the resonant wavelength of a high-$Q$ resonator can be measured accurately down to the picometre level, strain–optical coupling provides a sensitive measure of local strain in the multilayer structure. A series of flexible $Ge_{23}Sb_7S_{70}$ glass microdisk resonator samples with different SU-8 top and bottom cladding layer thickness combinations were fabricated and tested. By varying the cladding thickness, local strain at the microdisk resonators is modified when the samples are bent. This is apparent from Fig. 2a, where the resonant wavelength shift as a function of chip bending curvature is plotted for five different samples. The resonant wavelength shift was highly repeatable after several bending cycles, and little hysteresis was observed. Theoretical predictions based on classical multilayer bending theory as well as those made using our new multi-neutral-axis analysis are plotted in the same figure for comparison. Experimentally measured material moduli and strain–optic coefficients measured using the protocols outlined in Supplementary Section IV were used in the calculations. It is apparent that the classical theory fails to reproduce the experimentally observed trend, whereas our new theory successfully accounts for the strain–optical coupling behaviour. When we apply Supplementary equation (14) to convert the horizontal axis from the bending curvature in Fig. 2a to the bending-induced strain in Fig. 2b, all of the experimental data collapse onto one straight line, which verifies the linear dependence of the resonance peak shift on mechanical strain (equation (1)). The dramatic change of both the magnitude and sign of the resonance shift in different samples provides an effective method to control strain–optical coupling in flexible photonic devices and also has important practical implications. For applications where strain–optical coupling is undesirable, such as resonator refractometry sensing, the coupling can be nullified by strategically placing the device at the zero strain points. On the other hand, the coupling can be maximized when applied to photonic tuning or strain sensing.

NATURE PHOTONICS DOI: 10.1038/NPHOTON.2014.138

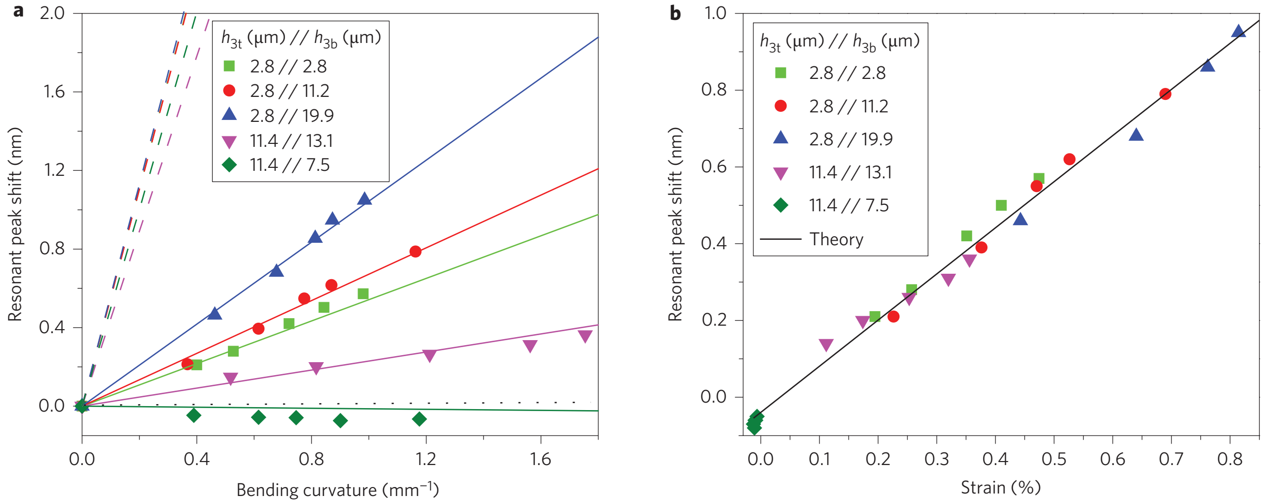


**Figure 2 | Strain–optical coupling in flexible photonic devices. a**, Resonance wavelength shift plotted as a function of bending curvature: each colour represents an SU-8 top/bottom cladding thickness combination. $h_{3t}$ and $h_{3b}$ denote the SU-8 top and bottom cladding thicknesses, as labelled in Supplementary Fig. 6a. Symbols are experimentally measured data, solid lines are predictions made using our analytical theory, and dashed lines are classical bending theory results. **b**, Resonance wavelength shift plotted as a function of bending strain, which can be calculated from the bending curvature using Supplementary equation (14). All data in Fig. 2b collapse to one curve, as predicted by equation (1).

The local neutral axis design imparts extreme mechanical flexibility to our devices. To test the mechanical reliability of the flexible devices, microdisk resonators were fabricated and their optical characteristics were measured after repeated bending cycles with a bending radius of 0.5 mm. As shown in Fig. 1f, there were minimal variations in both the quality factor and the extinction ratio after multiple bending cycles, demonstrating the superior mechanical robustness of the flexible devices. Our fatigue test, consisting of up to 5,000 bending cycles at a radius of 0.8 mm, resulted in a 0.5 dB $cm^{-1}$ increase in waveguide propagation loss and a 23% decrease in the resonator intrinsic *Q*-factor (Supplementary Section III). Optical microscopy further revealed no crack formation or interface delamination in the layers after 5,000 bending cycles (Supplementary Fig. 4).

## Adiabatic interlayer waveguide couplers

As our technology makes use of high-index ChGs as the backbone photonic materials, their amorphous nature further enables us to scale the fabrication method to 3D monolithic photonic integration on plastic substrates using multilayer deposition and patterning.

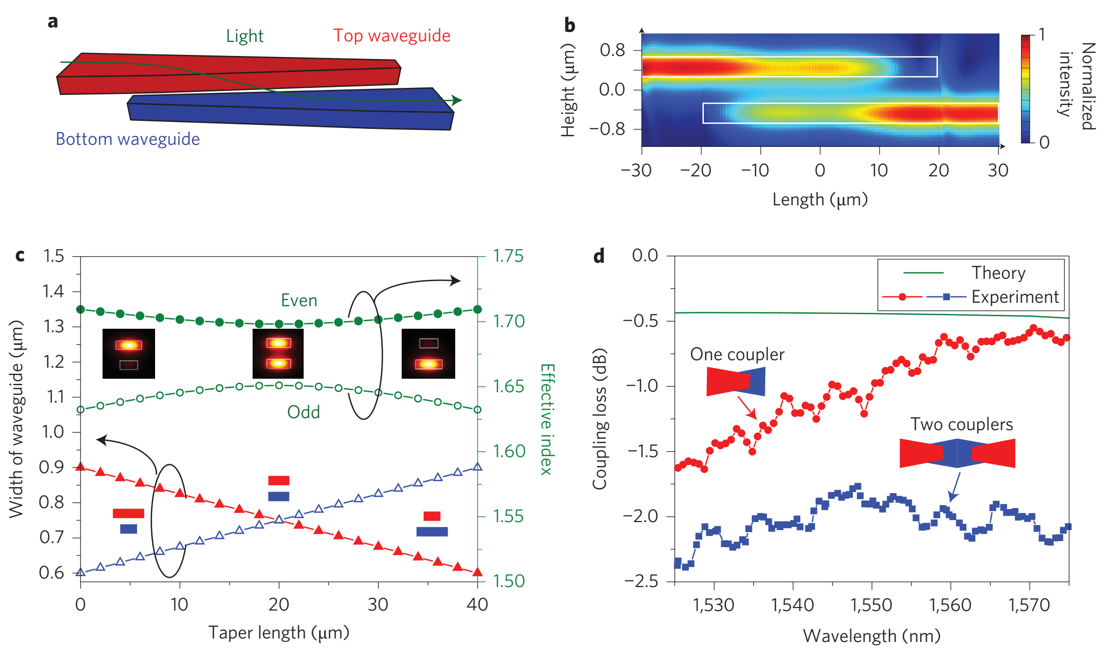


**Figure 3 | Adiabatic interlayer waveguide couplers. a**, Schematic structure of the interlayer waveguide coupler. **b**, Side view of steady-state optical field intensity distribution in the coupler, showing adiabatic power transfer from the top waveguide to the bottom waveguide. **c**, Top (red curve) and bottom (blue curve) waveguide widths and simulated supermode effective indices (green curves) in the taper section of the interlayer coupler. Insets: cross-sectional even supermode intensity profile evolution along the taper. **d**, FDTD simulated (green line) and measured (red and blue lines) transmission spectra of the interlayer coupler(s).

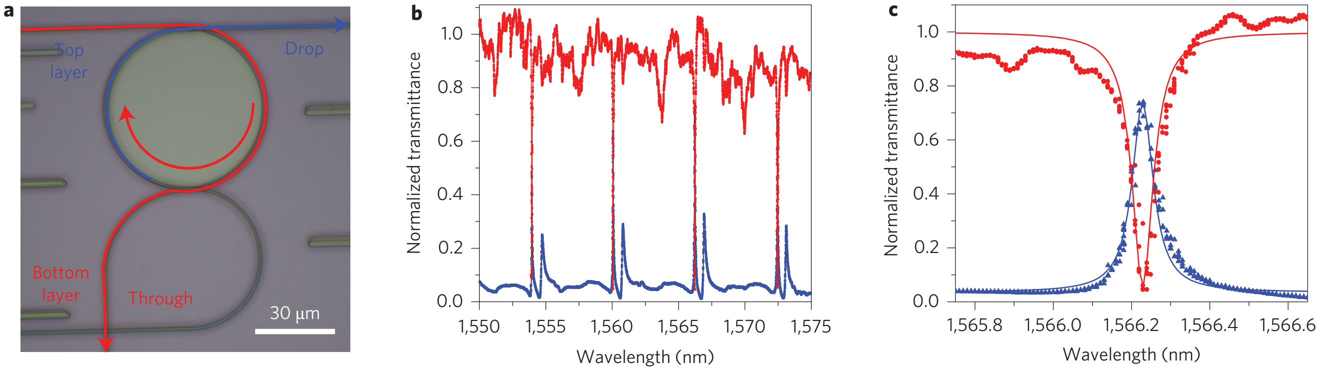


**Figure 4 | Vertically coupled add-drop resonator filter. a**, Optical microscope image of a two-layer vertically coupled resonator. **b**,**c**, Normalized transmission spectra of a vertically coupled resonator at its through (red) and drop (blue) ports. The device is designed to operate at the critical coupling regime near a wavelength of 1,550 nm. Symbols represent experimental data and lines are theoretical results calculated using a scattering matrix formalism.

The excellent planarization capability of ultrathin SU-8 resin ensures pattern fidelity in the multilayer process. This approach to 3D photonic structure fabrication offers a facile and simple alternative to conventional methods involving ion implantation[19], wafer bonding[17] or pick-and-place nanomanipulation[18]. Here, we demonstrate the fabrication of several important device building blocks, including broadband interlayer waveguide couplers, vertically coupled resonators and woodpile photonic crystals, using our approach. It is worth noting that all devices presented in this Article were fabricated using simple, low-cost ultraviolet contact lithography, without resorting to fine-line patterning tools such as electron-beam lithography or deep-ultraviolet lithography, and we expect significant device performance improvement through further optimization of the processing steps.

Figure 3a schematically shows the structure of an interlayer adiabatic waveguide coupler. The coupler consists of a pair of vertically overlapping inverse taper structures made of $Ge_{23}Sb_7S_{70}$ glass. The non-tapered waveguide sections are 0.9 μm wide and 0.4 μm high, designed for single quasi-transverse-electric mode operation at a wavelength of 1,550 nm. The device operates on the supermode adiabatic transformation principle[30,31], where light entering the coupler predominantly remains in the coupled waveguide system's fundamental mode. The simulated field mode intensity profiles of the coupled waveguides in the taper section are plotted in the insets to Fig. 4c. The effective indices of the even and odd modes were also plotted along the taper length. As shown in the figure, the even supermode, which is the fundamental mode of the coupled waveguide system, transitions adiabatically from the top waveguide to the bottom waveguide as the waveguide width changes in the taper section. Figure 3b shows a side view of the finite-difference time-domain (FDTD) simulated steady-state optical field intensity distribution in the coupler, which illustrates the power transfer process from the top waveguide to the bottom waveguide. Unlike traditional directional couplers based on phase-matched evanescent coupling, the adiabatic mode transformer coupler design is robust against fabrication error and wavelength dispersion. The adiabatic interlayer coupler exhibited broadband operation with 1.1 dB (single coupler) and 2.0 dB (double couplers) insertion loss (both averaged over a 50 nm band), comparable to the simulation results (0.5 dB loss per coupler) given the limited alignment accuracy of contact lithography and the waveguide sidewall roughness scattering loss (Fig. 3d).

## Vertically coupled add–drop resonator filter

Vertically coupled resonator add–drop filters were fabricated using the same approach on plastic substrates (Fig. 4a). The device consists of a microdisk resonator co-planar with the add waveguide, and a through-port waveguide in a second layer separated from the microdisk by a 550-nm-thick SU-8 layer. Unlike co-planar add–drop filters where the coupling strength has to be adjusted by changing the narrow gap width between the bus waveguides and the resonator, the critical coupling regime in vertical resonators is readily achieved by fine-tuning the thickness of the SU-8 separation layer. Figure 4c shows the normalized transmission spectrum of a resonator designed for critical coupling operation. The filter exhibited an insertion loss of 1.2 dB and a loaded $Q$-factor of $2.5 \times 10^4$ at both its through port and its drop port. These results agree well with our theoretical predictions made using a scattering matrix formalism[32] (Supplementary Section IX).

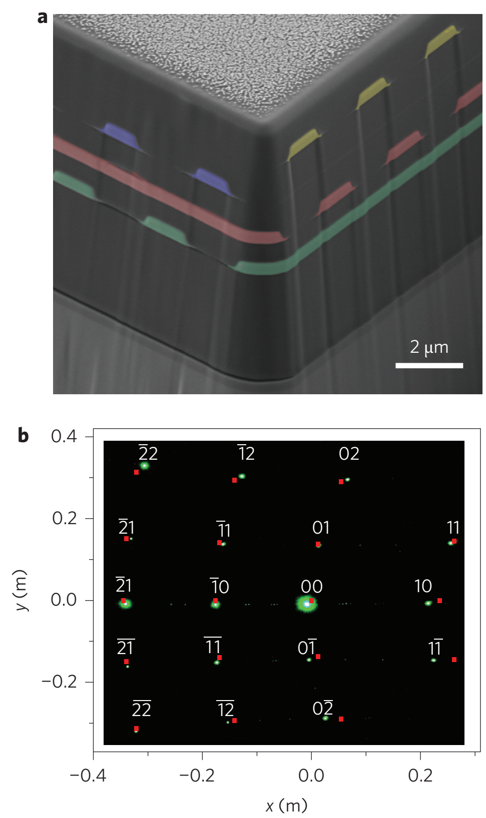


**Figure 5 | 3D woodpile photonic crystals. a**, Tilted focused ion beam-scanning electron microscopy view of a 3D woodpile photonic crystal (before delamination from the silicon handler substrate) showing excellent structural integrity. **b**, Diffraction patterns of a collimated 532 nm green laser beam from the photonic crystal. Red dots are diffraction patterns simulated using the Bragg diffraction equation.

### 3D woodpile photonic crystals

In addition to being used to fabricate two-layer devices such as interlayer couplers and vertically coupled resonator filters, our technique can be readily extended to the fabrication of multilayer structures that often present major challenges to conventional fabrication methods. As an example, Fig. 5a shows a tilted anatomy view of a four-layer woodpile photonic crystal fabricated using the method shown in Fig. 1a, before delamination from the handler substrate. The integrity and pattern fidelity of the photonic crystal structure were examined using optical diffraction. Figure 5b shows the diffraction spots from a collimated 532 nm green laser beam. The red dots in Fig. 5b represent the diffraction pattern calculated using Bragg equations (calculation details are presented in Supplementary Section IX), which matches nicely with the experimental results. The well-defined diffraction pattern indicates excellent long-range structural order of the photonic crystal.

In conclusion, we have experimentally demonstrated a simple and versatile method to fabricate high-index-contrast 3D photonic devices on flexible substrates. The method leverages the amorphous nature and low deposition temperature of novel ChG alloys to pioneer a 3D multilayer monolithic integration approach with dramatically improved device performance, processing throughput and yield. A new mechanical theory was developed and experimentally validated to accurately predict and control the strain–optical coupling mechanisms in the device. Guided by the multi-neutral axis theory, we have demonstrated mechanically robust devices with extreme flexibility, despite the inherent mechanical fragility of the glass film, and the devices can be twisted and bent to sub-millimetre radii without compromising their optical performance. The 3D monolithic integration technique, which is applicable to photonic integration on both traditional rigid substrates and non-conventional plastic substrates, is expected to open up new application venues such as high-bandwidth-density optical interconnects[33], conformal wearable sensors and ultrasensitive strain gauges.

## Methods

**Material and device fabrication.** Device fabrication was carried out at the University of Delaware Nanofabrication Facility. An SU-8 epoxy layer was first spin-coated onto the handler wafer, and a negative photoresist (NR9-1000PY, Futurrex) pattern was then lithographically defined on the SU-8 layer using contact lithography on an ABM Mask Aligner. ChG films were thermally evaporated onto the substrates from bulk glasses synthesized using a melt-quenching technique. Deposition was performed using a custom-designed system (PVD Products). The deposition rate was monitored in real time using a quartz crystal microbalance and was stabilized at 20 Å $s^{-1}$. After deposition, the sample was sonicated in acetone to dissolve the resist layer, leaving a glass pattern the reverse of the photoresist. The procedure was repeated several times to fabricate 3D structures. The fabricated glass devices were flood-exposed using a halogen lamp before optical testing to nullify the glass film's photosensitivity.

**Finite-element simulations.** Finite-element simulations were applied by ABAQUS 6.10 using plane strain elements (CPE4R) for the multilayer structure. In the experiment, the concave bending of the polyimide–silicone–SU-8 three-layer structure was induced through the buckling mode (Fig. 1d) instead of pure bending. With this concave bending the polyimide layer, which has a larger bending rigidity than the other two layers, is subject to the largest part of the bending moment, so the bending of the other two layers can be considered as being forced by the polyimide layer. To simulate this buckling-induced bending we applied rotation boundary conditions on the two ends of the polyimide layer, thereby generating curvatures the same as in the experiments at the middle point of the structure.

**Optical transmission measurements.** The optical transmission spectra of waveguides and resonators in the C and L bands were collected using a fibre end-fire coupling approach as shown in Supplementary Fig. 7a. Tapered lens-tip fibres were used to couple light from an external cavity tunable laser (Agilent 81682A) into and out of the waveguides through end facets formed by cleaving the samples before delamination from the silicon handler substrates. Supplementary Fig. 7b presents a far-field image of a quasi-transverse-electric guided mode output from a single-mode $Ge_{23}Sb_7S_{70}$ glass waveguide.

Received 26 July 2013; accepted 27 May 2014; published online 29 June 2014

## References


1. Ko, H. C. *et al.* A hemispherical electronic eye camera based on compressible silicon optoelectronics. *Nature* **454,** 748–753 (2008).
2. Kim, D.-H. *et al.* Epidermal electronics. *Science* **333,** 838–843 (2011).
3. Bosman, E. *et al.* Highly reliable flexible active optical links. *IEEE Photon. Technol. Lett.* **22,** 287–289 (2010).
4. Chen, Y., Li, H. & Li, M. Flexible and tunable silicon photonic circuits on plastic substrates. *Sci. Rep.* **2,** 622 (2012).
5. Yang, W. *et al.* Large-area InP-based crystalline nanomembrane flexible photodetectors. *Appl. Phys. Lett.* **96,** 121107 (2010).
6. Park, S.-I. *et al.* Printed assemblies of inorganic light-emitting diodes for deformable and semitransparent displays. *Science* **325,** 977–981 (2009).
7. Zhou, W. *et al.* Flexible photonic-crystal Fano filters based on transferred semiconductor nanomembranes. *J. Phys. D* **42,** 234007 (2009).
8. Xu, X. *et al.* Stamp printing of silicon-nanomembrane-based photonic devices onto flexible substrates with a suspended configuration. *Opt. Lett.* **37,** 1020–1022 (2012).
9. Ma, Z. *et al.* Fast flexible electronics based on printable thin mono-crystalline silicon. *ECS Trans.* **34,** 137–142 (2011).
10. Zablocki, M. J., Sharkawy, A., Ebil, O. & Prather, D. W. Nanomembrane transfer process for intricate photonic device applications. *Opt. Lett.* **36,** 58–60 (2011).
11. Fan, L. *et al.* Direct fabrication of silicon photonic devices on a flexible platform and its application for strain sensing. *Opt. Express* **20,** 20564–20575 (2012).
12. Bauters, J. F. *et al.* Ultra-low-loss high-aspect-ratio $Si_3N_4$ waveguides. *Opt. Express* **19,** 3163–3174 (2011).
13. Sandland, J. G. *Sputtered Silicon Oxynitride for Microphotonics: A Materials Study.* PhD thesis, Massachusetts Institute of Technology (2005).
14. Jaeyoun, K., Winick, K. A., Florea, C. & McCoy, M. Design and fabrication of low-loss hydrogenated amorphous silicon overlay DBR for glass waveguide devices. *IEEE J. Sel. Top. Quantum Electron.* **8,** 1307–1315 (2002).
15. Ma, Z. An electronic second skin. *Science* **333,** 830–831 (2011).
16. Kim, D.-H. *et al.* Stretchable and foldable silicon integrated circuits. *Science* **320,** 507–511 (2008).
17. Ishizaki, K., Koumura, M., Suzuki, K., Gondaira, K. & Noda, S. Realization of three-dimensional guiding of photons in photonic crystals. *Nature Photon.* **7,** 133–137 (2013).
18. Aoki, K. *et al.* Microassembly of semiconductor three-dimensional photonic crystals. *Nature Mater.* **2,** 117–121 (2003).
19. Koonath, P. & Jalali, B. Multilayer 3-D photonics in silicon. *Opt. Express* **15,** 12686–12691 (2007).
20. Sherwood-Droz, N. & Lipson, M. Scalable 3D dense integration of photonics on bulk silicon. *Opt. Express* **19,** 17758–17765 (2011).
21. Carlie, N. *et al.* Integrated chalcogenide waveguide resonators for mid-IR sensing: leveraging material properties to meet fabrication challenges. *Opt. Express* **18,** 26728–26743 (2010).
22. Hu, J. *et al.* Optical loss reduction in high-index-contrast chalcogenide glass waveguides via thermal reflow. *Opt. Express* **18,** 1469–1478 (2010).
23. DeCorby, R. G., Ponnampalam, N., Nguyen, H. T. & Clement, T. J. Robust and flexible free-standing all-dielectric omnidirectional reflectors. *Adv. Mater.* **19,** 193–196 (2007).
24. Abouraddy, A. F. *et al.* Towards multimaterial multifunctional fibres that see, hear, sense and communicate. *Nature Mater.* **6,** 336–347 (2007).
25. Petit, L. *et al.* Correlation between physical, optical and structural properties of sulfide glasses in the system Ge–Sb–S. *Mater. Chem. Phys.* **97,** 64–70 (2006).
26. Chauhan, R., Srivastava, A. K., Tripathi, A. & Srivastava, K. K. Linear and nonlinear optical changes in amorphous $As_2Se_3$ thin film upon UV exposure. *Prog. Nat. Sci. Mater. Int.* **21,** 205–210 (2011).
27. Ruan, Y., Jarvis, R. A., Rode, A. V., Madden, S. & Luther-Davies, B. Wavelength dispersion of Verdet constants in chalcogenide glasses for magneto-optical waveguide devices. *Opt. Commun.* **252,** 39–45 (2005).
28. Hu, J. *et al.* Planar waveguide-coupled, high-index-contrast, high-Q resonators in chalcogenide glass for sensing. *Opt. Lett.* **33,** 2500–2502 (2008).
29. Sun, J.-Y. *et al.* Inorganic islands on a highly stretchable polyimide substrate. *J. Mater. Res.* **24,** 3338–3342 (2009).
30. Yariv, A. in *Optical Electronics in Modern Communications* 526–531 (Oxford Univ. Press, 1997).
31. Sun, R. *et al.* Impedance matching vertical optical waveguide couplers for dense high index contrast circuits. *Opt. Express* **16,** 11682–11690 (2008).
32. Schwelb, O. Transmission, group delay, and dispersion in single-ring optical resonators and add/drop filters—a tutorial overview. *J. Lightwave Technol.* **22,** 1380–1394 (2004).
33. Li, L. *et al.* A fully-integrated flexible photonic platform for chip-to-chip optical interconnects. *J. Lightwave Technol.* **31,** 4080–4086 (2013).


## Acknowledgements

The authors thank S. Kozacik, M. Murakowski and D. Prather for assistance with device fabrication, N. Nguyen and M. Mackay for mechanical tests, N. Xiao and Y. Liu for assistance with optical measurement data processing, V. Singh for help with FIMMWAVE simulations and T. Gu and M. Haney for helpful discussions. L.L. acknowledges funding support from Delaware NASA/EPSCoR through a Research Infrastructure Development (RID) grant. H.L. and J.H. acknowledge funding support from the National Science Foundation (award no. 1200406). N.L. acknowledges start-up funding support from the Cockrell School of Engineering of the University of Texas, Austin. This work is based upon work supported in part by the National Science Foundation under cooperative agreement no. EEC-1160494. Any opinions, findings and conclusions or recommendations expressed in this material are those of the author(s) and do not necessarily reflect the views of the National Science Foundation.

## Author contributions

L.L. and H.L. conducted material synthesis, optical modelling, device fabrication and testing. S.Q. and N.L. performed mechanics modelling and analysis. Y.Z. assisted with film deposition and device characterization. J.H. conceived the device and structural designs. S. D., J.D.M. and K.R. contributed to material synthesis. J.H., N.L. and K.R. supervised and coordinated the project. All authors contributed to writing the paper.

## Additional information

Supplementary information is available in the online version of the paper. Reprints and permissions information is available online at www.nature.com/reprints. Correspondence and requests for materials should be addressed to J.H.

## Competing financial interests

The authors declare no competing financial interests.